Physics in Medicine & Biology

IPEM
Institute of Physics and Engineering in Medicine

PAPER

Data-driven respiratory phase-matched PET attenuation correction without CT

To cite this article: Donghwi Hwang *et al* 2021 *Phys. Med. Biol.* **66** 115009

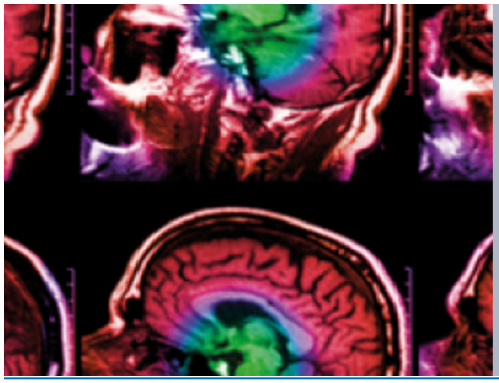

IOP Publishing Phys. Med. Biol. 66 (2021) 115009 https://doi.org/10.1088/1361-6560/abfc8f

Physics in Medicine & Biology

IPEM Institute of Physics and Engineering in Medicine

PAPER

Data-driven respiratory phase-matched PET attenuation correction without CT

RECEIVED
25 September 2020

REVISED
10 April 2021

ACCEPTED FOR PUBLICATION
28 April 2021

PUBLISHED
20 May 2021

Donghwi Hwang[1,2], **Seung Kwan Kang**[1,2], **Kyeong Yun Kim**[1,2], **Hongyoon Choi**[2], **Seongho Seo**[3] and **Jae Sung Lee**[1,2,4]

[1] Department of Biomedical Sciences, Seoul National University College of Medicine, Seoul, Republic of Korea
[2] Department of Nuclear Medicine, Seoul National University College of Medicine, Seoul, Republic of Korea
[3] Department of Electronic Engineering, Pai Chai University, Daejeon, Republic of Korea
[4] Institute of Radiation Medicine, Medical Research Center, Seoul National University College of Medicine, Seoul, Republic of Korea

E-mail: jaes@snu.ac.kr

Keywords: attenuation correction, data-driven gating, motion correction, simultaneous reconstruction

Supplementary material for this article is available online

Abstract

We propose a deep learning-based data-driven respiratory phase-matched gated-PET attenuation correction (AC) method that does not need a gated-CT. The proposed method is a multi-step process that consists of data-driven respiratory gating, gated attenuation map estimation using maximum-likelihood reconstruction of attenuation and activity (MLAA) algorithm, and enhancement of the gated attenuation maps using convolutional neural network (CNN). The gated MLAA attenuation maps enhanced by the CNN allowed for the phase-matched AC of gated-PET images. We conducted a non-rigid registration of the gated-PET images to generate motion-free PET images. We trained the CNN by conducting a 3D patch-based learning with 80 oncologic whole-body ^{18}F-fluorodeoxyglucose (^{18}F-FDG) PET/CT scan data and applied it to seven regional PET/CT scans that cover the lower lung and upper liver. We investigated the impact of the proposed respiratory phase-matched AC of PET without utilizing CT on tumor size and standard uptake value (SUV) assessment, and PET image quality (%STD). The attenuation corrected gated and motion-free PET images generated using the proposed method yielded sharper organ boundaries and better noise characteristics than conventional gated and ungated PET images. A banana artifact observed in a phase-mismatched CT-based AC was not observed in the proposed approach. By employing the proposed method, the size of tumor was reduced by 12.3% and $SUV_{90\%}$ was increased by 13.3% in tumors with larger movements than 5 mm. %STD of liver uptake was reduced by 11.1%. The deep learning-based data-driven respiratory phase-matched AC method improved the PET image quality and reduced the motion artifacts.

1. Introduction

Respiratory motion is a patient factor that degrades image quality and quantitative accuracy of positron emission tomography (PET). In addition, the anatomical mismatch between PET and computed tomography (CT) images due to different breathing patterns during PET and CT scans causes artifacts in the PET images corrected for attenuation and scatter based on CT-derived attenuation maps (e.g. banana artifacts shown in coronal PET slices) (Goerres *et al* 2003). PET quantification errors due to changes in lung density between the PET and CT images are also significant (Holman *et al* 2016).

The degradation of PET image quality due to the respiratory motion can be alleviated by employing a respiratory gating method that divides the respiratory cycle into multiple phases and sorts the acquired events into temporal bins (Werner *et al* 2009). However, the conventional respiratory-gated PET acquisition requires additional external devices to track the respiratory motion (e.g. RPM and Anzai belt). In addition, the gated PET images are noisier than ungated PET because of the smaller number of events collected in each temporal bin than

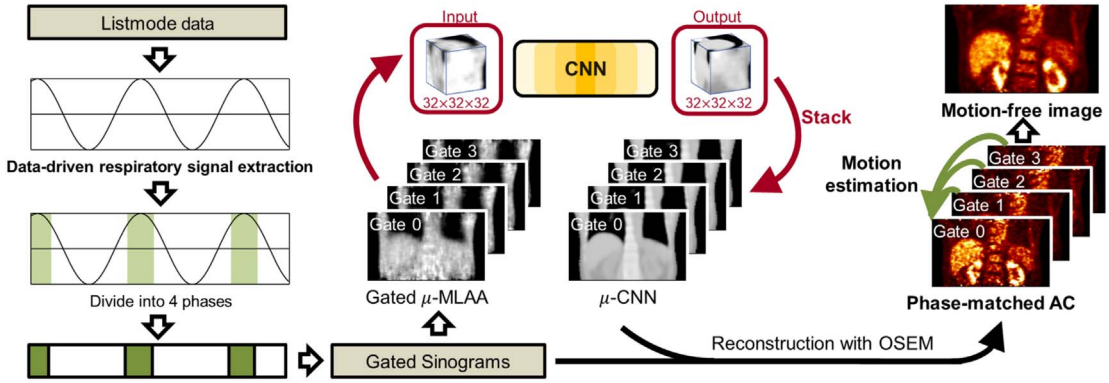

Figure 1. Data flow in the deep learning-based phase-matched attenuation correction method proposed in this study.

in total. To overcome the limitations of the external device-based respiratory gating methods, various data-driven approaches have been proposed (Schleyer *et al* 2009, Kesner *et al* 2014, Bertolli *et al* 2017, Ren *et al* 2017). As the data-driven gating methods estimate the respiratory motion based on the motion of radioactivity within a patient, their measurements are closely linked to the respiratory motion of organs (Walker *et al* 2019).

By estimating the motion vector field between the respiratory bins and performing non-rigid image registration using the estimated motion, we can employ all the events collected during the gated-PET acquisition and generate motion-free PET images (Bousse *et al* 2016, Lu *et al* 2018). To avoid the artifacts caused by the phase-mismatch between PET and CT, attenuation correction (AC) of the gated-PET images using phase-matched gated-CT is necessary (Nehmeh *et al* 2004a, 2004b, Luo *et al* 2008, Li *et al* 2009). However, external motion-tracking devices are required for gated-CT data acquisition that causes additional radiation exposure (Büther *et al* 2009). To address this issue, a simultaneous activity and attenuation estimation method was employed for phase-matched AC and motion estimation (Lu *et al* 2018). However, one of the limitations of the pioneering work was the potential errors in motion-estimating registration due to the high noise level of the simultaneously estimated activity images.

This study aims to develop a data-driven respiratory phase-matched gated-PET AC method that does not require the acquisition of CT at all. This method is also based on simultaneous activity and attenuation reconstruction improved by a deep neural network. The schematic of the proposed method is summarized in figure 1 and supplemental figure 1 (available online at stacks.iop.org/PMB/66/115009/mmedia). The respiratory cycle was estimated by calculating the centroid-of-distribution (COD) of detected events during the PET scan without an external motion-tracking device (Ren *et al* 2017). Gated activity and attenuation maps were then simultaneously reconstructed using maximum-likelihood reconstruction of attenuation and activity (MLAA) algorithm that requires solely the emission PET data (Rezaei *et al* 2012). High-quality gated attenuation maps were generated using a convolutional neural network (CNN) that was trained to predict a CT-derived attenuation map (μ-CT) from MLAA activity and attenuation maps (λ-MLAA and μ-MLAA) (Hwang *et al* 2018a, 2019a, Shi *et al* 2019). The CNN-enhanced attenuation map for each gating bin was used for the phase-matched PET attenuation and scatter correction. The corrected gated-PET activity images were used for a motion vector field estimation between the gating bins. Finally, motion-free PET images were generated using the estimated motion vector field.

We trained the CNN by conducting a 3D patch-based learning with 80 oncologic whole-body ^{18}F-fluorodeoxyglucose (^{18}F-FDG) PET/CT scan data and applied it to seven regional PET/CT scans that cover the lower lung and upper liver—the most vulnerable regions to the respiratory motion artifact. We further investigated the impact of the proposed respiratory phase-matched AC of PET without utilizing CT on tumor size and standard uptake value (SUV) assessment and PET image quality.

2. Materials and methods

2.1. Data set

For training the network, whole-body ^{18}F-FDG PET/CT scan data of 80 oncologic patients acquired using a Biograph mCT 40 scanner (effective timing resolution = 580 ps, Siemens Healthcare, Knoxville, TN) was retrospectively used which was same training and validation set used in our previous work (Hwang *et al* 2019b). In the PET scans, the upper body from head to upper thigh was scanned in 6–8 bed positions with a scan duration of 1 min/bed.

To evaluate the performance of the proposed method, the regional ^{18}F-FDG PET/CT scan data of seven oncologic patients (five male and two female, age $= 63.4 \pm 10.7$ years) acquired using the same PET/CT scanner were used. Patients were asked to hold the breath at the end-of-expiration during the CT acquisition. In these patients, listmode data was collected for 5 min in a bed position that includes lower lung and upper liver of each patient. The listmode data were histogrammed into four gated-sinograms (1.25 min each) as shown in figure 1. To generate the gated-sinograms, gating signals were estimated using a data-driven method described in the further section. Further, ungated sinograms were generated by integrating the entire 5 min data. Details on the data-driven gating are supplied in the next section.

For all the patients, PET/CT imaging was performed 60 min after intravenously injecting the ^{18}F- FDG (5.18 MBq kg^{-1}). The retrospective use and prospective acquisition of the scan data was approved by the Institutional Review Board of our institute and informed consent was obtained from all individual participants in this study.

2.2. Simultaneous image reconstruction

We reconstructed PET data sets using the MLAA with the TOF information (6 iterations and 21 subsets, 5 mm Gaussian post-filter) as described in our previous work (Hwang *et al* 2019a). To resolve the non-unique global scaling problem in the MLAA, the boundary constraint was applied during the attenuation image estimation in the MLAA (Rezaei *et al* 2012). For scatter correction in the MLAA, scatter sinogram was estimated from μ-CT using single scatter simulation (Watson *et al* 1996).

2.3. Data-driven respiratory signal measurement

The COD algorithm is a data-driven motion signal estimation method that requires no external device to measure the respiratory motion of patients (Ren *et al* 2017). Previous studies reported that the estimated motion signal using the COD method corresponds well with the external device-based methods (Ren *et al* 2017, Feng *et al* 2018). The COD indicates the center-of-mass of lines-of-response (LORs) measured within a specific PET field-of-view and time-bin. The COD is calculated as follows:

$$C_z = \frac{\sum Z_i}{N},$$

where Z_i is the center of LOR for each coincidence event in the axial direction and N is the total number of LORs. To extract the respiratory motion signal from the PET listmode data, a 100 ms long time-bin was used. The z-coordinate of COD (vertical motion in coronal and sagittal planes) was considered as the internal organs (and radiotracers within them) primarily move up and down owing to the respiration. We incorporated TOF information in the COD signal measurement to improve the accuracy of the COD method (Ren *et al* 2017).

Owing to the limited number of LORs measured in a short time-bin, noise level of the raw COD signal is high. Therefore, a band-pass filter that preserves 0.06–0.50 Hz frequency components was used for the raw COD signal to reduce statistical variation and baseline drift (Supplemental figure 2). From the filtered COD signal, breathing peaks were extracted to determine respiratory cycles. Each respiratory cycle (peak-to-peak) was divided into four gating windows with an even temporal length (figure 1). This phase-based gating approach was adopted in this study than the amplitude-based gating as the phase-based gating is insensitive to baseline drifts and other inaccuracies in the signal (Dawood *et al* 2007).

2.4. Network architecture and training

The CNN was designed to predict μ-CT from MLAA outputs (μ-MLAA and λ-MLAA) that are noisy and subject to crosstalk artifact (Hwang *et al* 2018a, 2019a). Inputs to the CNN were μ-MLAA and λ-MLAA in the form of $32 \times 32 \times 32$ matrix patches, and labels (ground-truth) were patches of the same size from μ-CT at the corresponding location. As shown in figure 1 and Supplemental figure 1, we employed a 3D U-net-based network with batch normalization. Certain convolutional layers preceded the U-net structure to reduce the noise in λ-MLAA where a patch-based intensity normalization using mean and variance of the patch was employed. No other preprocessing or normalization is applied on μ-MLAA. In the last layer that provides an output, $1 \times 1 \times 1$ convolution was used for scaling. Each convolution and deconvolution layer, except the last layer, was composed of $3 \times 3 \times 3$ kernels (supplemental figure 1). To prevent the CNN from learning geometric and systematic artifacts from the μ-CT, 3D patches for training the CNN were selected randomly rather than selected from the regular grid with even spacing. The 3D patches were employed for the CNN training if their centers are included in the body to avoid meaningless computation with blank patches. In addition, the MLAA outputs from the full iteration (iteration 6) and intermediate MLAA outputs from iterations 1–5 were used as the training set for the CNN to be more generalized and robust to various noise levels. Consequently, approximately 7.5 million patches were used for the CNN training.

To generate an output image with the trained network (μ-CNN), inferences from the input patches were stacked into the image matrix. As the inference for boundary voxels in a patch is not as accurate as that of the

center, 16 × 16 × 16 voxels at the center of 32 × 32 × 32 voxels were used for generating the μ-CNN. The cost function to train the network was L1-norm between the network output and μ-CT. The cost function was minimized using adaptive moment estimation algorithm (Kingma and Ba 2014). The size of mini-batch for accelerating the learning speed and improving the robustness in convergence was 64.

2.5. Additional activity image reconstruction

The gated-PET activity images were then reconstructed using an ordered-subset expectation-maximization algorithm (3 iterations and 21 subsets) where the μ-CNN was used for attenuation and scatter corrections. These gated-PET activity images were used for generating a motion-free PET image as described in the following section. For comparison, gated and ungated sinograms were also reconstructed using μ-CT.

2.6. Estimating motion vector field and non-rigid registration

For non-rigid image registration and motion-free image generation, we selected a gate bin (reference gate bin) where the μ-CNN is most similar to the μ-CT acquired at end-of-expiration while holding the breath. The similarity was measured using Dice similarity coefficient of the segmented lung regions in μ-CNN and μ-CT (Aasheim *et al* 2015, An *et al* 2016). The motion vector field from each gate bin to the reference bin was estimated using Elastix software (Klein *et al* 2010). In the Elastix, a B-spline transform is used for the motion field estimation, and mean squared errors between gate and reference bins are minimized using adaptive stochastic gradient descent algorithm. We used the logarithm of the PET activity images to estimate the motion vector field to reduce the registration error due to the large dynamic range and high noise level of the gated-PET images. Applying constraint on the motion vector fields by masking on patient's body prevented them from diverging outside the body. The mask was the union (U) of binary images derived from gated and statics images by applying intensity thresholds. This was clarified in the revised manuscript. Using the estimated motion vector fields, the activity images reconstructed using the μ-CNN for all gate bins were warped into the reference bin and averaged to generate a motion-free PET image.

2.7. Image analysis

The attenuation coefficient of the lungs at the end-of-expiration and end-of-inspiration were measured on the gated μ-CNN.

To evaluate the impact of the proposed method on the tumor size and SUV assessment and PET image quality, we drew volumes of interest (VOIs) on the PET activity images. VOIs were semi-automatically drawn on 24 suspected tumor regions with a movement higher than 5 mm in the seven patients by applying a threshold of 40% of maximum SUV in the tumor (SUV_{max}). The volume of VOIs (ml) was then calculated by multiplying the number of voxel in the VOI with the volume of each voxel. $SUV_{90\%}$ was determined by averaging the SUV of voxels with higher SUV than 90% of SUV_{max}. Additional VOIs were drawn on the relatively uniform region on the liver to evaluate %STD (the percentage ratio of standard deviation and mean value of PET activity in each VOI). For the comparison, tumor volume, $SUV_{90\%}$ and %STD in the gated PET images were also evaluated.

2.8. Comparison with other registration schemes

The proposed 'post-reconstruction registration' scheme was also compared to other schemes such as:

(1) Registration among attenuation-corrected gated PET using CT

(2) Registration among attenuation-corrected gated PET using MLAA without applying CNN

(3) Registration among non-attenuation-corrected gated PET

3. Results

3.1. Phase-matched AC

Figure 2 shows the μ-maps generated using the original MLAA and proposed method (μ-MLAA and μ-CNN, respectively) from a 5 min long ungated (left column) and 1.25 min long gated (middle columns) data. They were compared with μ-CT, the ground-truth (right column). Positions and outlines of the upper liver in μ-CNNs changed in accordance with the gate bin like respiratory motion (figures 2(a) and (b)). This implies that the extracted respiratory signal properly divided the list-mode data. The ungated and gated μ-CNN had lower noise levels and sharper boundaries than μ-MLAA. The high fluctuation of μ-values shown at both ends of axial FOV in the μ-MLAA was not observed in the μ-CNN. In addition, bone structures and soft organs were better identified in the μ-CNN.

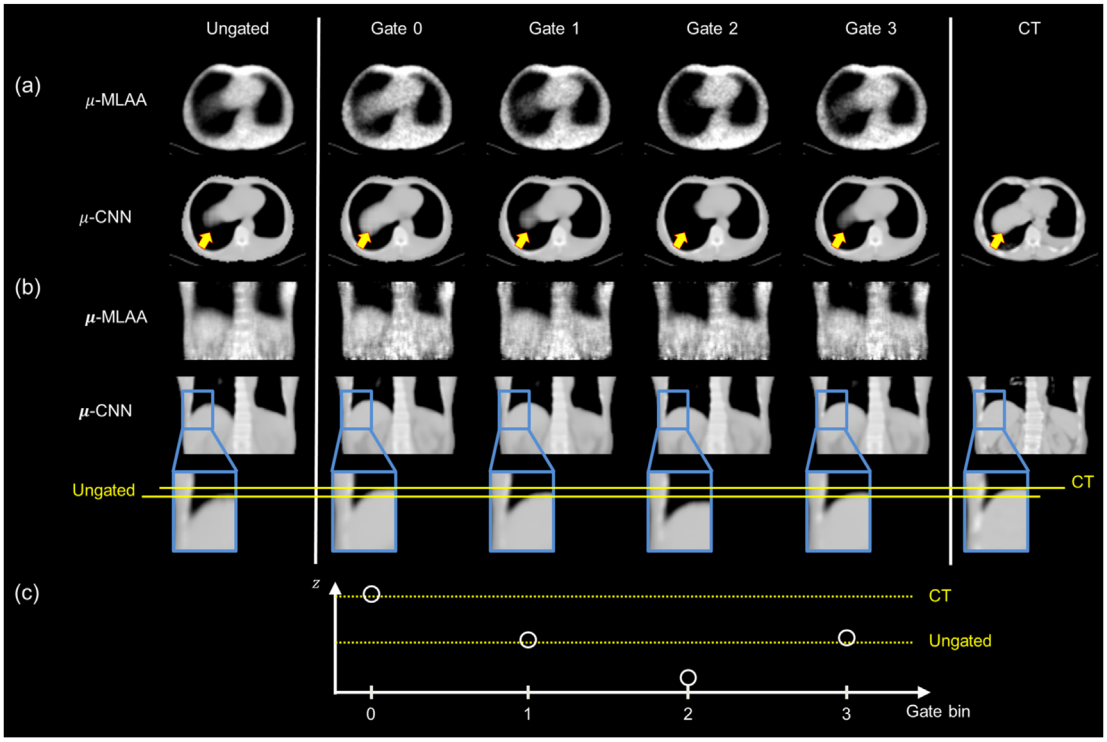

Figure 2. Attenuation maps generated using MLAA before and after CNN enhancement (μ-MLAA and μ-CNN, respectively) in (a) trans-axial and (b) coronal views. (c) Axial position (z) of the liver dome in each gate bin.

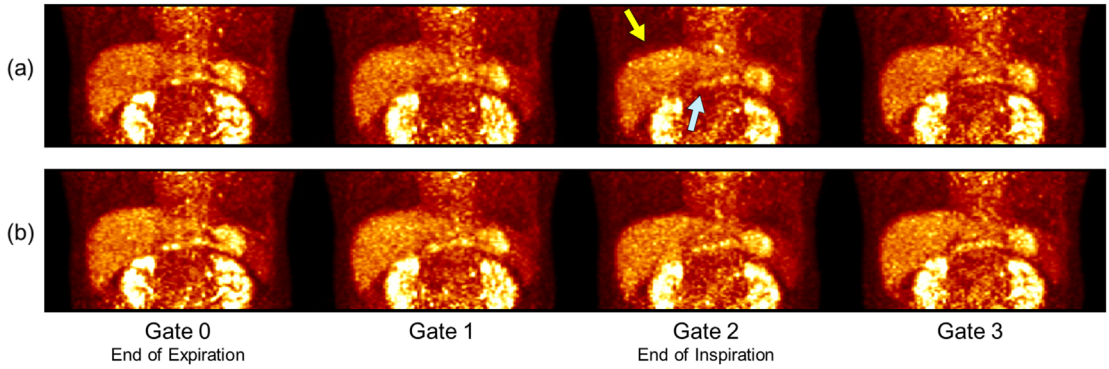

Figure 3. Maximum intensity projection images of the gated-PET corrected for attenuation and scatter using (a) phase-mismatched ungated μ-CT and (b) phase-matched gated μ-CNN.

The noise level in the gated μ-CNN was not inferior to that of the ungated μ-CNN and μ-CT. In addition, the boundaries of soft organs (e.g. kidneys) were better resolved in the gated μ-CNN compared with the ungated μ-MLAA and μ-CNN. The axial position of the liver dome in the ungated μ-CNN was different from the μ-CT because CT was acquired during breath-hold at the end-of-expiration, but the emission PET data were acquired during the respiratory period (figure 2(b)). Contrarily, one of the four-gated μ-CNNs always corresponded well with the μ-CT (e.g. Gate 0 in figure 2) and used as the reference gate bin for the following motion correction. Figure 3 shows the maximum intensity projection images of the gated PET corrected for attenuation and scatter using (A) μ-CT and (B) gated μ-CNN. The banana artifact shown in the phase-mismatched CT-based AC (figure 3(a)) that is the most evident at the end of inspiration (yellow arrow) is not observed in the phase-matched gated μ-CNN approach (figure 3(b)). The non-uniform activity in the stomach at the boundary between fat and soft tissue which is observed in the CT-based AC at the end of inspiration (sky-blue arrow) is also mitigated by the gated μ-CNN. The lung cancer lesions shown in μ-CT were also well represented in the gated μ-CNN images (arrows in figure 4). In addition, changes in the lung attenuation coefficient according to the respiratory phase were observed (figure 5(a)). At the end-of-inspiration, the lung volume is expected to be greater than at the end-of-expiration. Because the total mass of lung tissue must be preserved, the lung density

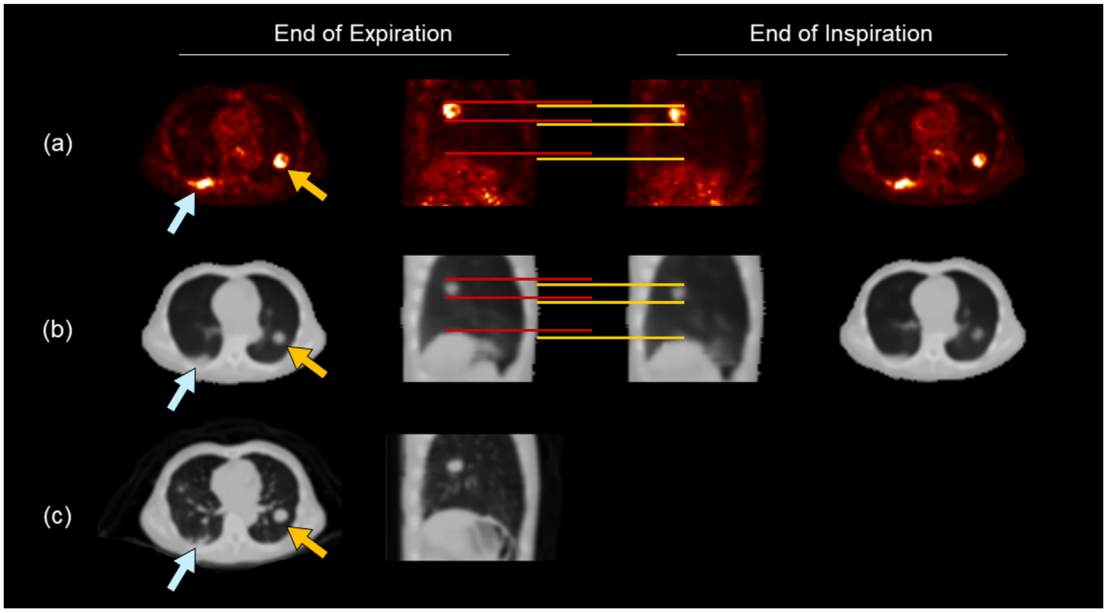

Figure 4. Lung cancer lesions and their movement according to respiratory phase observed in (a) gated PET and (b) phase-matched gated μ-CNN in end-of-expiration and end of inspiration. (c) μ-CT.

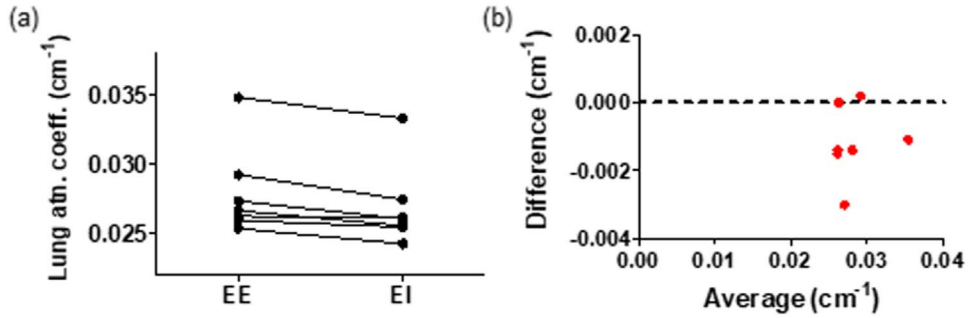

Figure 5. Lung measurements in μ-CNN. Changes in (a) attenuation coefficient between end-of-expiration (EE) and end-of-inspiration (EI). (b) Bland-Altman plot for mean lung attenuation coefficient of phase-matched gated μ-CNN and μ-CT at the end-of-expiration.

and attenuation coefficients at end-of-inspiration are expected to be smaller than at end-of-expiration, which is consistent with what Shaker *et al* (2004) reported.

The difference in the lung attenuation coefficient between μ-CT and μ-CNN at the end-of-expiration was less than 6% except for a case who yielded 11% difference (figure 5(b)).

3.2. Motion-free image generation

In figure 6, 5 min long ungated PET images are overlaid on CT. The ungated PET image that is conventionally used without phase-matched AC and motion compensation showed significant position mismatch between PET and CT in addition to the motion artifact at organ boundaries (figure 6(a)). However, these problems were mitigated by the proposed deep learning-based phase-matched AC without using CT, followed by the non-rigid motion correction (figure 6(b)). When an author who is a nuclear medicine physician (Choi HY) has examined all the output of motion corrections, there was no remarkable artificial creation of small lesions with high activity (i.e. false positives) or the suppression of signal (i.e. false negatives).

The motion-free PET corrected with attenuation and respiratory motion using the phase-matched gated μ-CNN improved the lesion detectability and enhanced the uptake quantification for small tumors as shown in figure 7 and Supplemental figure 3. In the conventional ungated PET images, tumors indicated by yellow arrows were stretched along the axial direction due to the respiratory motion. On the contrary, the tumors shown in the proposed motion-free PET images featured smaller size and higher activity. The results of the quantitative analysis on the %STD, $SUV_{90\%}$, and tumor size are plotted in figure 8. By employing the proposed method, the

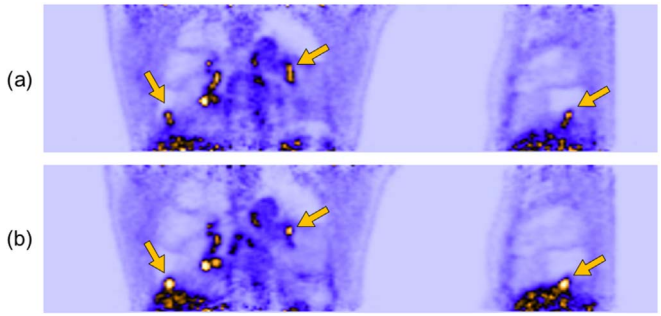

Figure 6. Mitigated respiratory motion artifact and PET/CT mismatch obtained by the proposed method. (a) Conventional ungated PET without phase-matched attenuation correction and motion compensation. (b) Motion-free PET corrected for attenuation and respiratory motion using phase-matched gated μ-CNN and data-driven motion-tracking method.

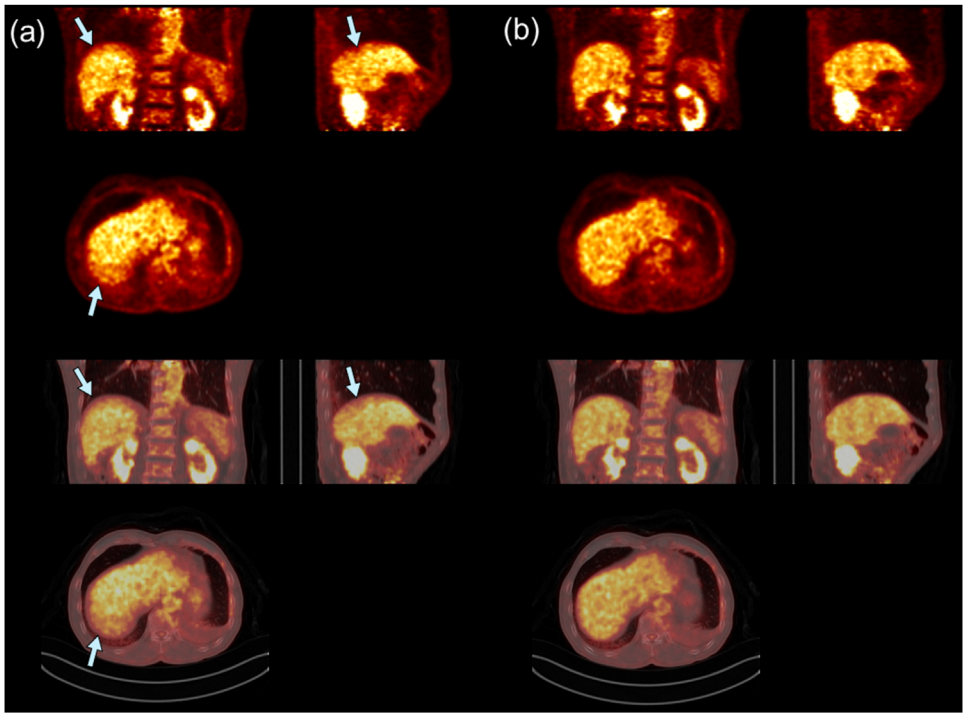

Figure 7. Improved lesion detectability and enhanced uptake quantification of the proposed method. (a) Conventional ungated PET without phase-matched attenuation correction and motion compensation. (b) Motion-free PET corrected for attenuation and respiratory motion using phase-matched gated μ-CNN and data-driven motion-tracking method.

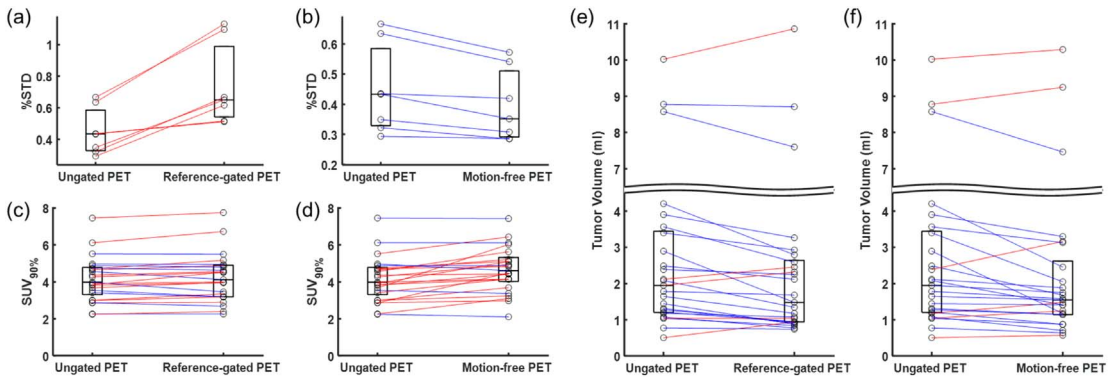

Figure 8. Change of %STD of liver uptake, $SUV_{90\%}$ in tumor, and tumor volume by employing the proposed phase-matched attenuation correction and respiratory motion correction compared with ungated PET. Incremental change is colored red and the contrary is colored blue.

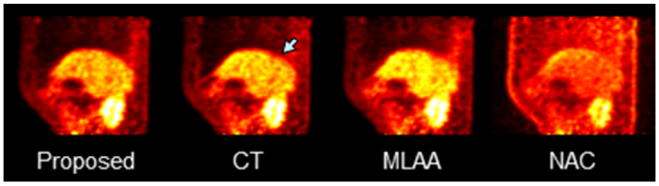

Figure 9. Comparison of post-reconstruction registration schemes using different attenuation correction methods.

tumor size measurement was reduced by 12.3% and $SUV_{90\%}$ was increased by 13.3% in tumors with higher movements than 5 mm. On the other hand, the tumor size measurement was reduced by 11.3% and $SUV_{90\%}$ was increased by only 1.8% in reference gated PET. In the uniform region in the liver, %STD was reduced by 11.1% in the proposed method while the reference gated PET showed 120% increase in %STD.

3.3. Comparison with other registration scheme

Figure 9 shows the motion-free images generated by applying different post-reconstruction registration schemes in a representative case. The anatomical mismatch in CT-based AC resulted in the banana artifact (blue arrow). The liver activity in the original MLAA approach without applying CNN was significantly higher than that of proposed and CT-based approaches.

4. Discussion

Patient motion correction without an external motion-tracking device is one of the most active research areas of PET imaging because wearing fiducial markers or Anzai belt for motion tracking is time-consuming and uncomfortable (Slipsager *et al* 2019). The COD method employed in this study is a promising approach to the device-less estimation of linear motion (Ren *et al* 2017). In this study, the vertical motion of internal organs in the chest and abdomen owing to the respiration was estimated using the COD method enhanced by TOF information and band-pass filtering. The estimated COD signal was useful for the phase-based gate-binning of the list-mode data. Although the phase-based gating yields uniform statistical noise characteristics and MLAA reconstruction performance across the gating bins (figures 2 and 3), this method would be less robust than the amplitude-based approach to the patients with irregular breathing. Further investigation on the impact of the gating methods on MLAA estimation, CNN-filtering, and motion-free PET generation will be necessary.

One of the limitations of this study that we conducted the MLAA reconstruction with the scatter distribution estimated from μ-CT. Iterative methods to estimate the scatter distribution during the MLAA reconstruction were recently proposed (Rezaei *et al* 2019, Li *et al* 2020). However, the additional computation time required for the repeated scatter estimation would hinder their practical use. One of the more practical ways we are considering is the deep learning-based scatter estimation incorporated into the MLAA.

Also, the lack of a convincing gold standard is the main limitation of this proof-of-concept study. Either breath-hold PET which is hard for standard PET systems or a high count single-gated reference is a more convincing gold standard. In addition, a dynamic CT rather than a breath-hold CT can offer a good means to assess the deformed CT map.

Another limitation is that ungated PET and CT images were used for the CNN training that was applied to the gated PET data. Because we performed patch-based learning, major data used for the network training came from other regions rather than lung and upper liver that are vulnerable to the position mismatch due to respiration in ungated PET/CT (Hwang *et al* 2019a, 2019b). In addition, the noise level of gated PET tested in this study would be similar to the training data set because the scan times for each frame of the gated PET and ungated PET were 1.25 and 1.0 min, respectively.

The small number of respiratory-gated PET scan datasets used for the performance evaluation of the proposed method is another limitation of this study. Because it is quite small to produce sufficient evidence of the method working well and systematically on many occasions, further investigations with a larger number of subjects are necessary.

In almost all medical image processing topics including segmentation, registration, and restoration, the deep learning method is rapidly implemented (Choi 2018, Gong *et al* 2018, Kang *et al* 2018, Kim *et al* 2018, Park *et al* 2018, Guo *et al* 2019, Hegazy *et al* 2019, Kale *et al* 2019, Lee *et al* 2019, Lee 2021). AC of PET using pseudo-CT transformed from magnetic resonance imaging (MRI) is one of the most active deep learning research topics in medical image generation (Liu *et al* 2017, Leynes *et al* 2018, Arabi *et al* 2019, Bradshaw *et al* 2018, Spuhler *et al*

2019, Torrado-Carvajal *et al* 2019). However, the primary disadvantage of the MRI-based PET AC is that converting MRI to CT using deep learning may not be physically and biologically relevant as the physical quantity measured by the two modalities is not closely related (Vandenberghe and Marsden 2015, Yoo *et al* 2015, Lee 2021). Our deep learning-based enhancement of the attenuation map reconstructed using simultaneous PET activity and attenuation reconstruction algorithm, such as MLAA, would have better rationale than MRI-based approaches as this approach does not rely on cross-modal image transform (Hwang *et al* 2019a). Moreover, our approach has been validated for several PET radiotracers including ^{18}F-FDG, ^{18}F-FP-CIT, and ^{68}Ga-DOTATOC (Hwang *et al* 2018a, 2019a, 2019b). This approach has been used to combine the attenuation maps from MLAA and Dixon MRI (Hwang *et al* 2018b). Thus, this attenuation map has the potential to replace the MRI-based AC for future generations of TOF PET/MR scanners (Hwang *et al* 2018a).

Further, we showed that our approach to enhance the MLAA attenuation map using a deep learning technique was useful for the phase-matched AC in the respiratory gating PET. The improved attenuation map can also be effective in improving the performance of other simultaneous reconstruction based data-driven motion correction methods (Lu *et al* 2018). The phase-matched AC is regarded necessary but impractical because of the increased radiation dose from the gated-CT. Although not proven, our approach has the potential to be superior to the gated CT-based phase-matched AC. This is because the patient motion and different breathing patterns between PET and CT scans can cause another type of position mismatch artifact in a gated-CT based approach (Lu *et al* 2018, Nehmeh *et al* 2004a).

Deep learning-based approaches, even if they can produce impressive results, need to be evaluated rigorously because we don't have to trust them unless clearly explained (Antun *et al* 2020). However, it is impossible to validate a deep learning-based approach using all possible different datasets. One of the efforts we have made to ensure the stability of the proposed method is the sanity check we performed in the previous work (figure 5 in Hwang *et al* 2019b). In addition, the attenuation maps generated using MLAA and CNN enabled more accurate AC in patients with metallic implants (figure 30 in Lee 2021). Although training set included CT images with metal artifacts, CNN was not susceptible to the metal artifacts.

In this study, CNN trained and validated with ungated PET data performed well with the gated PET data. There is concern that CNN may learn the systematic mismatches between MLAA and CT at the lung and liver boundaries. However, The number of unmatched patch is relatively small, which prevents the CNN from learning the mismatch. The relatively large difference between the activity images corrected for attenuation using μ-CNN and μ-CT at the lung and liver boundaries shown in our earlier work (figure 6 in Hwang *et al* 2019b) supports this idea.

There is an impact of motion in PET quantification not only due to the mismatch of emission and attenuation and but also because of the attenuation value change with respiration (Shaker *et al* 2004, Holman *et al* 2016). Our proposed phase-matched attenuation maps also showed the change in attenuation coefficients (figure 5(a)). The difference between the gated μ-CNN at the end-of-expiration and μ-CT was less than 6% except for a case. In the exceptional case with 11% difference, only a small portion of the lungs (approximately 10% volume) was included in the PET image, leading to the statistical variation in μ-value calculation.

The gated activity images corrected for attenuation with phase-matched attenuation maps using the proposed method were integrated after the non-rigid registration to generate motion-free PET (Polycarpou *et al* 2012, Tsoumpas *et al* 2013). The motion-free P*ET* allows for better SNR and lesion detectability than the gated-PET that includes a smaller number of PET counts. The image-registration based motion-free image generation is not a new approach. However, the anatomical image-guided PET motion correction has been rarely investigated in PET/CT because of the lack of gated-CT. Therefore, utilizing the gated activity and attenuation maps together for motion vector field estimation would be an approach that can achieve more robust motion correction. Furthermore, we should evaluate the feasibility of the proposed method in gated and dynamic cardiac PET scans.

5. Conclusion

We have developed a deep learning-based data-driven respiratory phase-matched AC method. As the COD method enables successful extraction of respiratory signals and the CNN generates high-quality phase-matched attenuation maps from MLAA outputs, the proposed method improved the PET image quality while mitigating the motion artifacts.

ORCID iDs

Jae Sung Lee https://orcid.org/0000-0001-7623-053X

References

Aasheim L B, Karlberg A, Goa P E, Haberg A, Sorhaug S, Fagerli U-M and Eikenes L 2015 PET/MR brain imaging: evaluation of clinical UTE-based attenuation correction *Eur. J. Nucl. Med. Mol. Imaging* **42** 1439–46

An H J, Seo S, Kang H, Choi H, Cheon G J, Kim H-J, Lee D S, Song I C, Kim Y K and Lee J S 2016 MRI-based attenuation correction for PET/MRI using multiphase level-set method *J. Nucl. Med.* **57** 587–93

Antun V, Renna F, Poon C, Adcock B and Hansen A C 2020 On instabilities of deep learning in image reconstruction and the potential costs of AI *Proc. Natl Acad. Sci. USA* **117** 30088–95

Arabi H, Zeng G, Zheng G and Zaidi H 2019 Novel adversarial semantic structure deep learning for MRI-guided attenuation correction in brain PET/MRI *Eur. J. Nucl. Med. Mol. Imaging* **46** 2746–59

Bertolli O, Arridge S, Wollenweber S D, Stearns C W, Hutton B F and Thielemans K 2017 Sign determination methods for the respiratory signal in data-driven PET gating *Phys. Med. Biol.* **62** 3204–20

Bradshaw T H, Zhao G, Jang H, Liu F and McMillan A B 2018 Feasibility of deep learning-based PET/MR attenuation correction in the pelvis using only diagnostic MR images *Tomography* **4** 138–47

Bousse A, Bertolli O, Atkinson D, Arridge S, Ourselin S, Hutton B F and Thielemans K 2016 Maximum-likelihood joint image reconstruction/motion estimation in attenuation-corrected respiratory gated PET/CT using a single attenuation map *IEEE Trans. Med. Imaging* **35** 217–28

Büther F, Dawood M, Stegger L, Wubbeling F, Schafers M, Schober O and Schafers K P 2009 List mode-driven cardiac and respiratory gating in PET *J. Nucl. Med.* **50** 674–81

Choi H 2018 Deep learning in nuclear medicine and molecular imaging: current perspectives and future directions *Nucl. Med. Mol. Imaging.* **52** 109–18

Dawood M, Büther F, Lang N, Schober O and Schäfers K P 2007 Respiratory gating in positron emission tomography: a quantitative comparison of different gating schemes *Med. Phys.* **34** 3067–76

Feng T, Wang J, Sun Y, Zhu W, Dong Y and Li H 2018 Self-gating: an adaptive center-of-mass approach for respiratory gating in PET *IEEE Trans. Med. Imaging* **37** 1140–8

Goerres G W, Burger C, Kamel E, Seifert B, Kaim A H, Buck A, Buehler T C and Schulthess G K 2003 Respiration-induced attenuation artifact at PET/CT: technical considerations *Radiology* **226** 906–10

Gong K, Guan J, Liu C-C and Qi J 2018 PET image denoising using a deep neural network through fine tuning *IEEE Trans. Radiat. Plasma. Med. Sci.* **3** 153–61

Guo Z, Li X, Huang H, Guo N and Li Q 2019 Deep learning-based image segmentation on multimodal medical imaging IEEE Trans. Radiat. Plasma *Med. Sci.* **3** 162–9

Hegazy M A A, Cho M H, Cho M H and Lee S Y 2019 U-net based metal segmentation on projection domain for metal artifact reduction in dental CT *Biomed. Eng. Lett.* **9** 375–85

Holman B F, Cuplov V, Hutton B F, Groves A M and Thielemans K 2016 The effect of respiratory induced density variations on non-TOF PET quantitation in the lung *Phy. Med. Biol.* **61** 3148–63

Hwang D, Kim K Y, Kang S K, Seo S, Paeng J C, Lee D S and Lee J S 2018a Improving the accuracy of simultaneously reconstructed activity and attenuation maps using deep learning *J. Nucl. Med.* **59** 1624–9

Hwang D, Kim K Y, Kang S K, Seo S and Lee J S 2018b Generation of attenuation map for whole-body PET/MRI using a deep neural network applied to simultaneously reconstructed activity and attenuation and Dixon MRI *Proc. IEEE Nucl. Sci. Symp. Med. Imaging. Conf.*

Hwang D, Kim K Y, Kang S K, Choi H, Seo S, Paeng J C, Lee D S and Lee J S 2019a Accurate attenuation correction for whole-body Ga-68-DOTATOC PET studies using deep learning *J. Nucl. Med.* **60** 568

Hwang D, Kang S K, Kim K Y, Seo S, Paeng J C, Lee D S and Lee J S 2019b Generation of PET attenuation map for whole-body time-of-flight 18F-FDG PET/MRI using a deep neural network trained with simultaneously reconstructed activity and attenuation maps *J. Nucl. Med.* **60** 1183–9

Kale V V, Hamde S T and Holambe R S 2019 Multi class disorder detection of magnetic resonance brain images using composite features and neural network *Biomed. Eng. Lett.* **9** 221–31

Kang S K, Seo S, Shin S A, Byun M S, Lee D Y, Kim Y K, Lee D S and Lee J S 2018 Adaptive template generation for amyloid PET using a deep learning approach *Hum. Brain. Mapp.* **39** 3769–78

Kesner A L, Schleyer P J, Büther F, Walter M A, Schäfers K P and Koo P J 2014 On transcending the impasse of respiratory motion correction applications in routine clinical imaging—a consideration of a fully automated data driven motion control framework *EJNMMI Phys.* **1** 1–11

Kim J Y, Suh H Y, Ryoo H G, Oh D, Choi H, Paeng J C, Cheon G J, Kang K W and Lee D S 2018 Amyloid PET quantification via end-to-end training of a deep learning *Nucl. Med. Mol. Imaging.* **53** 340–8

Kingma D and Ba J 2014 Adam: a method for stochastic optimization *Proc. Int. Conf. Learn. Represent.* arXiv:1412.6980

Klein S, Staring M, Murphy K, Viergever M A and Pluim J P 2010 Elastix: a toolbox for intensity-based medical image registration *IEEE Trans. Med. Imaging* **29** 196–205

Lee M S, Hwang D, Kim J H and Lee J S 2019 Deep-dose: a voxel dose estimation method using deep convolutional neural network for personalized internal dosimetry *Sci. Rep.* **9** 10308

Lee J S 2021 A review of deep learning-based approaches for attenuation correction in positron emission tomography *IEEE Trans. Radiat. Plasma Med. Sci.* **5** 160–84

Leynes A P, Yang J, Wiesinger F, Kaushik S S, Shanbhag D D, Seo Y, Hope T A and Larson P E Z 2018 Zero-echo-time and dxon deep pseudo-CT (ZeDD CT): direct generation of pseudo-CT images for pelvic PET/MRI attenuation correction using deep convolutional neural networks with multiparametric MRI *J. Nucl. Med.* **59** 852–8

Li R, Lewis J H, Cerviño L I and Jiang S B 2009 4D CT sorting based on patient internal anatomy *Phys. Med. Biol.* **54** 4821–33

Li Y, Matej S and Karp J S 2020 Practical joint reconstruction of activity and attenuation with autonomous scaling for time-of-flight PET *Phys. Med. Biol.* **65** 1–19

Liu F, Jang H, Kijowski R, Bradshaw T and McMillan A B 2017 Deep learning MR imaging-based attenuation correction for PET/MR imaging *Radiology* **286** 676–84

Lu Y *et al* 2018 Respiratory motion compensation for PET/CT with motion information derived from matched attenuation-corrected gated PET data *J. Nucl. Med.* **59** 1480–6

Luo Z, Xi Z, Wang J and Tang D 2008 Sorting 4DCT images based on manifold learning *Proc. ICICTA* **2008** 181–5

Nehmeh S A *et al* 2004a Four-dimensional (4D) PET/CT imaging of the thorax *Med. Phys.* **31** 3179–86

Nehmeh S A *et al* 2004b Quantitation of respiratory motion during 4D-PET/CT acquisition *Med. Phys.* **31** 1333–8

Park J, Hwang D, Kim K Y, Kang S K, Kim Y K and Lee J S 2018 Computed tomography super-resolution using deep convolutional neural network *Phys. Med. Biol.* **63** 145011

Polycarpou I, Tsumpas C and Marsden P K 2012 Analysis and comparison of two methods for motion correction in PET imaging *Med. Phys.* **39** 6474–83

Ren S, Jin X, Chan C, Jian Y, Mulnix T, Liu C and Carson R E 2017 Data-driven event-by-event respiratory motion correction using TOF PET list-mode centroid of distribution *Phys. Med. Biol.* **62** 4741–55

Rezaei A, Defrise M, Bal G, Michel C, Conti M, Watson C and Nuyts J 2012 Simultaneous reconstruction of activity and attenuation in time-of-flight PET *IEEE Trans. Med. Imaging* **31** 2224–33

Rezaei A, Schramm G, Willekens S M A, Delso G, Laere K V and Nuyts J 2019 A quantitative evaluation of joint activity and attenuation reconstruction in TOF PET/MR brain imaging *J. Nucl. Med.* **60** 1649–55

Schleyer P J, O'Doherty M J, Barrington S F and Marsden P K 2009 Retrospective data-driven respiratory gating for PET/CT *Phys. Med. Biol.* **54** 1935–50

Shaker S B, Dirksen A, Laursen L C, Skovgaard L T and Holstein-Rathlou N H 2004 Volume adjustment of lung density by computed tomography scans in patients with emphysema *Acta. Radiol.* **45** 417–23

Shi L, Onofrey J A, Revilla E M, Toyonaga T, Menard D, Ankrah J, Carson R E, Liu C and Lu Y 2019 A novel loss function incorporating imaging acquisition physics for PET attenuation map generation using deep learning *Proc. Med. Image. Comput. Comput. Assist. Interv.* **11767** 723–31

Slipsager J M *et al* 2019 Markerless motion tracking and correction for PET, MRI, and simultaneous PET/MRI *PLoS One* **14** 1–17

Spuhler K D, Gardus J, Gao Y, DeLorenzo C, Parsey R and Huang C 2019 Synthesis of patient-specific transmission data for PET attenuation correction for PET/MRI neuroimaging using a convolutional neural network *J. Nucl. Med.* **60** 555–60

Torrado-Carvajal A, Vera-Olmos J, Izquierdo-Garcia D, Catalano O A, Morales M A, Margolin J, Soricelli A, Salvatore M, Malpica N and Cantana C 2019 Dixon-VIBE deep learning (DIVIDE) pseudo-CT synthesis for pelvis PET/MR attenuation correction *J. Nucl. Med.* **60** 429–35

Tsoumpas C, Polycarpou I, Thielemans K, Buerger C, King A P, Schaeffter T and Marsden P K 2013 The effect of regularization in motion compensated PET image reconstruction: a realistic numerical 4D simulation study *Phys. Med. Biol.* **58** 1759–73

Vandenberghe S and Marsden P K 2015 PET-MRI: a review of challenges and solutions in the development of integrated multimodality imaging *Phys. Med. Biol.* **60** R115–54

Walker M D, Morgan A J, Bradley K M and McGowan D R 2019 Evaluation of data-driven respiratory gating waveforms for clinical PET imaging *EJNMMI Res.* **9** 1–10

Watson C C, Newport D and Casey M E 1996 A single scatter simulation technique for scatter correction in 3D PET *Three-Dim. Imag. Recon. Rad. Nucl. Med.* **4** 255–68

Werner M K, Parker J A, Kolodny G M, English J R and Palmer M R 2009 Respiratory gating enhances imaging of pulmonary nodules and measurement of tracer uptake in FDG PET/CT *AJR Am. J. Roentgenol.* **193** 1640–5

Yoo H J, Lee J S and Lee J M 2015 Integrated whole body MR/PET: where are we? *Korean J. Radiol.* **16** 32–49